Geophysical Research Letters

RESEARCH LETTER
10.1029/2023GL104016

Characterization of Icy Moon Hydrospheres Through Joint Inversion of Gravity and Magnetic Field Measurements

Flavio Petricca[1], Antonio Genova[1], Julie C. Castillo-Rogez[2], Marshall J. Styczinski[2], Corey J. Cochrane[2], and Steven D. Vance[2]

[1]Department of Mechanical and Aerospace Engineering, Sapienza University of Rome, Rome, Italy, [2]Jet Propulsion Laboratory, California Institute of Technology, Pasadena, CA, USA

Key Points:

- We developed a technique to combine measurements of gravity and magnetic field that improves the characterization of icy moon hydrospheres
- We applied this joint inversion to constrain Europa's ice and ocean thicknesses with gravity and magnetic induction data from Galileo
- Our results demonstrate that the joint inversion of these observations allows us to better understand the hydrosphere's structure

Supporting Information:

Supporting Information may be found in the online version of this article.

Correspondence to:

F. Petricca,
flavio.petricca@uniroma1.it

Citation:

Petricca, F., Genova, A., Castillo-Rogez, J. C., Styczinski, M. J., Cochrane, C. J., & Vance, S. D. (2023). Characterization of icy moon hydrospheres through joint inversion of gravity and magnetic field measurements. *Geophysical Research Letters*, *50*, e2023GL104016. https://doi.org/10.1029/2023GL104016

Received 5 APR 2023
Accepted 15 AUG 2023

Abstract Several bodies in the outer solar system are believed to host liquid water oceans underneath their icy surfaces. Knowledge of the hydrosphere properties is essential for understanding and assessing their habitability. We introduce a methodology based on Bayesian inference that enables a robust characterization of the hydrosphere through the combination of gravity and magnetic induction data. The interior models retrieved are consistent with the geophysical observations, leading to probability distributions for the relevant interior properties. We apply this joint inversion approach to constrain Europa's hydrosphere with gravity and magnetic field measurements acquired by the Galileo mission. Our results indicate that the combination of these datasets allows simultaneous constraints on the ice shell and ocean thickness, enhancing our knowledge of the hydrosphere structure. This methodology is valuable for synergistic interior science investigations of several missions in development or in planning, including Europa Clipper, JUICE and the Uranus Orbiter and Probe.

Plain Language Summary The outer solar system has several moons with icy surfaces that may hide oceans of liquid water beneath them. Studying these oceans is important for assessing whether these worlds can harbor life. We have developed a novel technique to study these potentially habitable oceans by combining measurements of the gravity and magnetic fields of these icy moons. We use a statistical method to generate models of the moon's interior that are consistent with the available gravity and magnetic field measurements. By applying this method to measurements of Jupiter's moon, Europa, we show that it can provide robust estimates of the thicknesses of the moon's ice shell and the subsurface ocean. This new technique will be useful for studying the interior of Europa and other icy moons with the data acquired by future missions, such as Europa Clipper, JUICE, and the Uranus Orbiter and Probe.

1. Introduction

Icy moons are prime targets in programs of space exploration because of the potential habitability of their subsurface oceans. Available data confirm the existence of liquid oceans for several moons of Jupiter and Saturn. Induced magnetic fields detected by the magnetometer onboard Galileo at Europa (Khurana et al., 1998; Kivelson et al., 2000) and possibly Callisto (Khurana et al., 1998) provide evidence of salty water layers at depth. Available magnetic measurements and auroral observations for Ganymede are consistent with induction in a subsurface ocean, but the interpretation is complicated by the presence of an internal permanent dynamo (Kivelson et al., 2002; Saur et al., 2015). Because the induced magnetic field amplitude and phase are functions of the ocean thickness and conductivity, and the ice shell thickness, induction data can be analyzed to characterize the hydrosphere of icy moons. The analysis of the induction signature in the magnetic field measurements is therefore a powerful technique for sounding the interior of icy moons. Additional constraints on the interior can be derived from gravity measurements. The analysis of radio tracking data has provided the mass and moment of inertia (MoI) of icy moons, including Europa (Anderson et al., 1998; Gomez Casajus et al., 2021), Ganymede (Anderson et al., 1996; Gomez Casajus et al., 2022) and Titan (Durante et al., 2019; Iess et al., 2010), that constrain the moons' density structures (e.g., Kuskov & Kronrod, 2005; Sohl et al., 2002).

Inversions based on gravity data only, however, are degenerate because of the similar density between ice and water. Single-frequency magnetic induction measurements, on the other hand, preclude unambiguous characterization of the hydrosphere properties because of the trade-off between the ocean depth, ocean conductivity and ice thickness in determining the induction response. An independent analysis of these measurement types is thus insufficient to characterize the ice shell and the ocean, resulting in large uncertainties in the hydrosphere

structure (e.g., Anderson et al., 1998; Zimmer et al., 2000). Combining the two datasets is therefore key to improve the interior structure inversion.

We present a technique for the characterization of icy moon interiors based on Bayesian inference and the joint inversion of gravity and magnetic induction measurements. The resulting interior models are consistent with the combined observations. The relevant interior properties are treated as free parameters and varied randomly to generate probability distributions for the value of each property. This methodology is applied to the interior structure of Europa by analyzing available gravity and magnetic induction data acquired by the Galileo mission (i.e., Schilling et al., 2004; Gomez Casajus et al., 2021).

2. Data and Methods

Our inversion methodology is based on a Markov-chain Monte Carlo (MCMC) algorithm (e.g., Genova et al., 2019; Matsuyama et al., 2016; Ruesch et al., 2019). We build upon the method previously applied to the inversion of Mercury's interior from gravity data by Genova et al. (2019). Biersteker et al. (2023) developed a novel methodology for the inversion of multi-frequency magnetic induction measurements based on Bayesian inference. These authors applied it to synthetic data for the Europa Clipper Magnetometer, showing its potential for retrieving the hydrosphere properties. Our approach is new because we self-consistently handle both gravity and magnetic induction models. In this way, we estimate the interior properties by generating models in simultaneous agreement with gravity and magnetic field observations. We apply this technique to the inversion of Europa's interior from available gravity and magnetic induction data acquired by Galileo.

2.1. Gravity Data

Measurements of Europa's static gravity field from the analysis of Galileo radio science data yields the moon's mass and MoI, which yield estimates of the hydrosphere thickness: mass $M = 4.79982 \pm 0.00062 \times 10^{22}$ kg, normalized MoI $C/MR^2 = 0.346 \pm 0.005$ (Anderson et al., 1998). A recent reanalysis of the Galileo data provided a significantly higher MoI: $C/MR^2 = 0.3547 \pm 0.0024$ (Gomez Casajus et al., 2021). We adopt the latter value in our analysis to study the interior of Europa. We also carried out further analyses by assuming the MoI reported by Anderson et al. (1998) to test and validate our method.

2.2. Magnetic Induction Data

The induced magnetic field of Europa can be used to constrain the radii of the ocean–mantle and ocean–ice interfaces, and the ocean electrical conductivity. The magnetic field sensed by Europa oscillates in the frame of the moon, primarily at Jupiter's rotation rate relative to the moon (the "synodic" period; Seufert et al., 2011). The field also oscillates at Europa's orbital period due to the orbital eccentricity and inclination and to the day-night and dawn-dusk asymmetries of the magnetosphere. In response, electrical currents are induced in the conductive ocean, generating an induced magnetic field. The induction response is sensitive to the radial distance of the ocean boundaries from the moon's center of mass and dissolved salt content. The magnetic field near Europa was measured during most flybys of the Galileo spacecraft. An induction amplitude of $A = 0.97 \pm 0.02$ was derived by fitting an induced magnetic dipole moment to the data acquired during four flybys (Schilling et al., 2004), where $A = 1.0$ is equivalent to a perfect conductor with a radius equal to Europa's. This near-perfect induction response was obtained by using simplified models for the magnetospheric plasma and driving field. Given the smaller magnitude of the driving field variations at Europa's orbital period and the limited amount of data available, the only contribution to the driving field was assumed to be at the synodic frequency. In subsequent work, Hand and Chyba (2007) noted that such a high induction amplitude is difficult to reconcile with thermodynamic models that balance radiogenic heating in the mantle, tidal heat generation in the ice shell, and the heat radiated to space from the surface, which are consistent with ~20–30 km thick shell (Howell, 2021; Hussmann et al., 2002; Ojakangas & Stevenson, 1989; Tobie et al., 2005). As noted by Hand and Chyba (2007), an ice thickness consistent with expectations (>20–30 km) requires $A < 0.92$. Therefore, we consider models with $A = 0.97 \pm 0.02$ and this lower value for comparison ($A = 0.92 \pm 0.02$). The formal uncertainty reported by Schilling et al. (2004) may be optimistic because it assumes that measurement errors are negligible. However, errors arising from mismodeling of plasma interactions may increase this uncertainty. We then also consider models consistent with 3 times the quoted uncertainty.

Table 1
Free Parameters Explored in the Markov-Chain Monte Carlo Inversion of the Interior Structure

Parameter	Units	Step	Range
Core radius r_{core}	km	25	0–1,000[a,b]
Core density ρ_{core}	kg m^{-3}	50	5,150–8,000[a]
Mantle density ρ_{mantle}	kg m^{-3}	25	2,500–4,500[a,b,c]
Ocean thickness d_{ocean}	km	5	0–200[d]
Ocean density ρ_{ocean}	kg m^{-3}	5	1,000–1,300
Ice shell thickness d_{shell}	km	2.5	0–200[e]

Note. The parameter space is bounded to prevent the generation of physically inconsistent models. Electrical conductivity is derived from the ocean density by assuming different chemical compositions.

[a]Anderson et al. (1998). [b]Kuskov and Kronrod (2005). [c]Gomez Casajus et al. (2021). [d]Hand and Chyba (2007). [e]Howell (2021).

2.3. Interior Structure Modeling

Most of the models applied to interpret gravity and induction response measurements are based on a two- or three-layer structure (Anderson et al., 1998; Gomez Casajus et al., 2021; Hand & Chyba, 2007). Our modeling is based on a four-layer, fully differentiated Europa, accounting for a metallic core, a rocky mantle, an ocean, and an ice shell. Our parameter space includes the density and thickness of each layer (Table 1), except for the density of the ice layer, assumed to be equal to pure water ice (917 kg m^{-3}; Fukusako, 1990), while the radial extent of the mantle is derived from the total body radius R and the thicknesses of the other layers. All the free parameters are explored in order to generate interior models that match the observed mass, MoI and induction amplitude. Each parameter is randomly initialized by the MCMC algorithm and perturbed within certain bounds that prevent the generation of physically inconsistent models (Table 1).

All the models are spherically symmetric, enabling an evaluation of gravity and induction parameters from analytic expressions. The mass M and MoI C are computed as:

$$M = \frac{4}{3}\pi \sum_{i=0}^{3} \rho_i \left(r_{i+1}^3 - r_i^3\right), \tag{1}$$

$$C = \frac{8}{15}\pi \sum_{i=0}^{3} \rho_i \left(r_{i+1}^5 - r_i^5\right), \tag{2}$$

where ρ_i is the density of the ith layer, r_i are the radii of the interfaces between the different layers and r_0 is equal to zero. The induced magnetic field is modeled by assuming that the ice shell and deep interior are non-conductive, and the ocean is uniformly conducting with conductivity σ (e.g., Zimmer et al., 2000). As noted by Zimmer et al. (2000), the ice is assumed to be non-conductive because its conductivity is greater than ∼10 mS/m only if it contains a substantial amount of melt. Similarly, the conductivity of the mantle rocks is low (on the order of ∼10 mS/m as measured for the Earth's mantle; Parkinson, 1983) and it does not significantly affect the induction response (Hand & Chyba, 2007; Zimmer et al., 2000). Although the electrical conductivity of an iron core may be several orders of magnitude higher than the ocean conductivity (∼1.5×10^6 S/m measured at Earth's core conditions; Pozzo et al., 2012), the core is expected to produce a very small induction signature at the synodic frequency (<1% for the range of Europa's ocean thickness resulting from the cases analyzed in this study, i.e., >70 km; Seufert et al., 2011). This small contribution occurs due to the attenuation of the driving signal as it propagates through the ocean, and the further attenuation of the induced signal as it propagates back.

The induced magnetic field can be described by the amplitude A and phase delay ϕ of the induced field with respect to the response that characterizes a perfectly conducting sphere with the moon's radius R (1560.8 km). These parameters are computed as (e.g., Vance et al., 2021):

$$Ae^{-i\phi} = \left(\frac{r_{ocean}}{R}\right)^3 \frac{j_2(kr_{mantle})y_2(kr_{ocean}) - j_2(kr_{ocean})y_2(kr_{mantle})}{j_0(kr_{ocean})y_2(kr_{mantle}) - j_2(kr_{mantle})y_0(kr_{ocean})}, \tag{3}$$

$$k = \sqrt{i\omega\mu_o\sigma} \tag{4}$$

where j_m, y_m are the spherical Bessel functions of first and second kind of order m; r_{ocean} is the radius of the ice–ocean interface, and r_{mantle} is the radius of the rocky mantle–ocean interface. This formulation is based on the spherical Bessel functions (Styczinski et al., 2022) rather than on the standard Bessel functions (e.g., Hand & Chyba, 2007; Zimmer et al., 2000). The wavenumber k is related to the penetration depth of the magnetic field inside the conducting ocean and depends on its electrical conductivity σ and on the angular frequency of oscillation of the driving field ω. Refer to Text S1 in Supporting Information S1 for further details on the forms of k and Equation 3. Although the frequency spectrum of the Jupiter's driving field contains the frequencies associated with the synodic and orbital periods, their harmonics, and beats between these, we only focus on the synodic period (11.23 hr) as it is the only one considered in published constraints by Schilling et al. (2004).

To model the induced magnetic field, we compute the ocean conductivity and salinity from the ocean density, which is a free parameter in our modeling, by using published experimental data for an assumed composition. A broad range of compositions has been suggested for Europa's ocean, including a seawater composition with mainly NaCl (Zolotov & Shock, 2001), an ocean dominated by $MgSO_4$ (Hand & Chyba, 2007; Kargel et al., 2000), and compositions accounting for a significant presence of carbonates (Castillo-Rogez et al., 2022). To better understand the effects of the ocean modeling on our inversion, we modeled each of these three compositions. Available experimental data on the relationships between density, salinity, and conductivity are obtained from the literature for the ocean models composed of seawater (Equation 9 from Poisson (1980) and Equations 5a–5c from Millero et al. (2008) evaluated at $T = 0°C$), $MgSO_4$ (Equation 2 and Figure 1 from Hand and Chyba (2007) and Figure 1 and Table 1 from Abdulagatov et al. (2007)) and the carbonate-rich composition (Supplementary Material from Castillo-Rogez et al. (2022)). We use the experimental curves provided in these studies to compute the salinity and conductivity for each density and model the magnetic induction amplitude.

2.4. Inversion Methodology

Our methodology is based on a MCMC algorithm (e.g., Genova et al., 2019; Ruesch et al., 2019) that estimates the properties of the interior by generating models that are consistent with the gravity and magnetic field observations. We explore a large parameter space with the Metropolis–Hastings algorithm (Hastings, 1970; Metropolis et al., 1953). We generate interior models in chains, starting with a random model and randomly sampling the parameter space. As the results may depend on the selection of the initial model, we generate 30 distinct chains. The initial model of each chain is selected by sampling the prior distributions, which are assumed to be uniform distributions for each parameter across the ranges provided in Table 1. The draws are independent, leading to a different starting point for each chain. The proposal distributions for the properties of interest are assumed to be Gaussian, with a mean of zero and a standard deviation (called "step" in Table 1) adjusted to thoroughly explore the parameter space. The burn-in of each chain (i.e., number of models discarded at the beginning of each chain to avoid biases in the final distributions) is set to 10,000. The convergence of the chains is tested with the Gelman–Rubin statistics by using a threshold of 1.01 for the potential scale reduction factor (PSRF; Gelman and Rubin (1992)). We terminate the chains when 50,000 models per chain are accepted, yielding a satisfactory PSRF for all the observations. The average acceptance fraction ranges from 3% to 5% of the evaluated models for all the chains.

The results presented below are reported in terms of central value (the mode of the distribution) and 68% credible intervals. The credible intervals are determined through the highest posterior density method, which selects the shortest possible interval in which the parameter falls with a certain probability (e.g., ∼68% or 1-standard-deviation level).

3. Results

Previous inferences of Europa's hydrosphere from gravity data, assuming a three-layer structure, yielded a hydrosphere thickness from 80 to 170 km (Anderson et al., 1998). The analysis by Gomez Casajus et al. (2021) constrained two-layer models of Europa with the updated MoI, yielding a hydrosphere 138.7 ± 7.7 km thick. We validate our methodology by constraining the interior of Europa with the mass and MoI provided by both studies and comparing the derived hydrosphere thickness. We derive a hydrosphere thickness of 160^{+25}_{-25} km based on our four-layer models and the MoI by Anderson et al. (1998). Models using the more recent MoI by Gomez Casajus et al. (2021) result in a hydrosphere 136^{+16}_{-17} km thick. This latter estimate is consistent with that derived for the two-layer model by Gomez Casajus et al. (2021). Our uncertainties are larger because we adjust a larger number of parameters that accounts for correlations between the layer properties. This correlation leads to a more robust assessment of the uncertainties on the derived quantities by yielding a probability density function for each adjusted parameter. The study by Anderson et al. (1998) is based on a parametric analysis of end-member models that accounts for rock densities between 3,000 kg m^{-3} and ∼3,800 kg m^{-3}, suggesting a hydrosphere thickness range of 80–170 km. By exploring a broader parameter space compared to previous studies, including rock densities up to 4,500 kg m^{-3}, thicker hydrospheres are expected as confirmed by our results. Figure 1 and Figure S1 in Supporting Information S1 show the histograms of the hydrosphere thickness obtained by constraining the modeling with the MoI by Gomez Casajus et al. (2021) and by Anderson et al. (1998), respectively.

Since the MoI is not significantly sensitive to the relatively low density contrast between ice (∼917 kg m^{-3}) and water (∼1,000 kg m^{-3}), the properties of the ice shell and the ocean cannot be disentangled with gravity

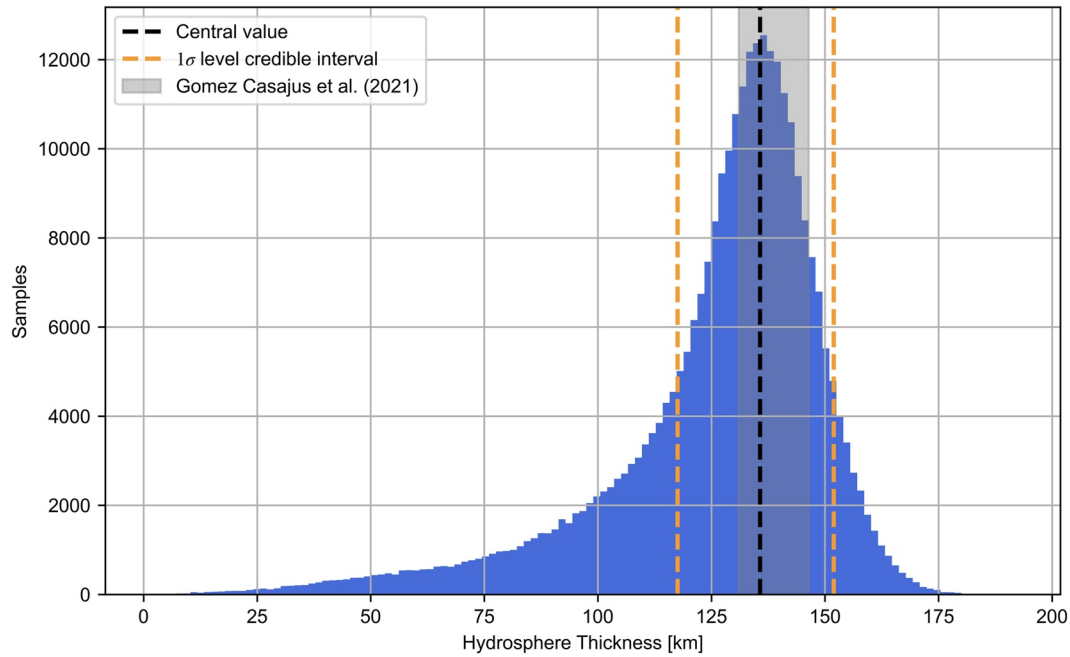

Figure 1. Histogram of the hydrosphere thickness that we retrieve by constraining our inversion only with gravity data from Gomez Casajus et al. (2021). The resulting thickness is 136^{+16}_{-17} km, consistent with previous inferences by Gomez Casajus et al. (2021), represented by the gray shaded area.

measurements only. The inversion based on single-frequency magnetic induction data only is also degenerate because of the trade-offs between the ice thickness, ocean depth, and conductivity in determining the induction response. Our approach allows us to break this degeneracy by generating interior models that are simultaneously consistent with the gravity and magnetic induction observations. This is illustrated here through the combination of the mass and MoI retrieved by Gomez Casajus et al. (2021) with the induction amplitude estimated by Schilling et al. (2004). As shown in Figure 2, while inversions based solely on gravity (Figure 2a) or magnetic induction (Figure 2b) measurements cannot separately constrain the properties of the ice shell and the ocean, our joint inversion simultaneously constrains the thicknesses of both layers (Figure 2c). The majority of the resulting models are characterized by a thin shell and a deep ocean. The thickness of the ice layer is estimated to be 4^{+8}_{-3} km and the ocean depth is 133^{+21}_{-34} km. Our estimate of the ice thickness is consistent with the value obtained by Hand and Chyba (2007), who constrained Europa's interior with the induction amplitude by Schilling et al. (2004) and showed that it requires an ice thickness of ∼4 km. This finding disagrees with expectations from thermal models, which suggest a ∼20–30 km thick shell (Howell, 2021; Ojakangas & Stevenson, 1989). This discrepancy is likely due to the high induction amplitude (Schilling et al., 2004), which was derived by assuming that the only contributions from magnetospheric plasma is due to the Alfvén wing currents. Factoring in plasma contributions in a more detailed model would affect the induction amplitude. Additionally, accounting for contributions from Jupiter's driving field at multiple frequencies may affect the derived induction amplitude. To produce an ice thickness consistent with predictions from thermal modeling (>20–30 km), the induction amplitude cannot be greater than $A = 0.92$ as suggested by Hand and Chyba (2007). We show the effects of a lower estimate by applying our methodology to this value in Figure S2 of Supporting Information S1. We derive a shell thickness of 24^{+11}_{-12} km. The corresponding ocean depth is 111^{+21}_{-30} km. We performed additional analyses to account for possible errors in the formal uncertainty reported by Schilling et al. (2004). We analyzed cases with $A = 0.97 \pm 0.06$ (Figure S3 in Supporting Information S1, the derived ice and ocean thicknesses are 4^{+27}_{-3} km and 123^{+24}_{-43} km, respectively) and with $A = 0.92 \pm 0.06$ (Figure S4 in Supporting Information S1, the derived ice and ocean thicknesses are 24^{+27}_{-21} km and 105^{+32}_{-45} km, respectively).

The results shown in Figure 2 are based on the assumption of a seawater composition for Europa's ocean. The assumed type of salts dissolved in the ocean influences the derived structure of the hydrosphere by determining the ocean electrical conductivity. We tested the effects of the assumed ocean composition on the inversion of

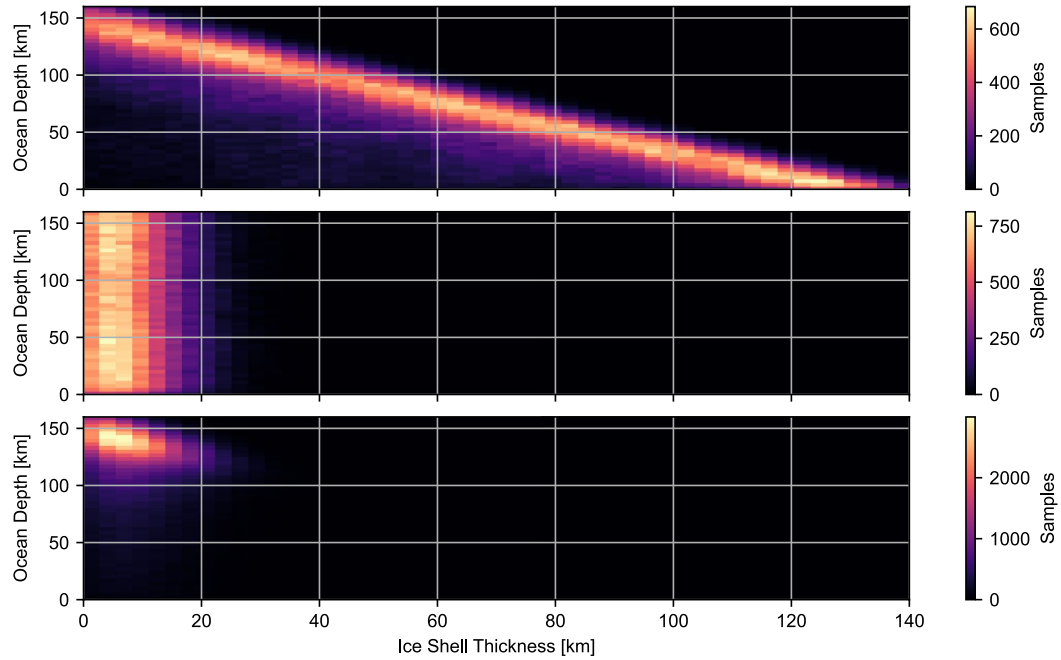

Figure 2. Histograms for ocean and ice shell thicknesses obtained through (a) inversion of gravity data only from Gomez Casajus et al. (2021), (b) inversion of magnetic induction data only from Schilling et al. (2004), (c) joint inversion of gravity and magnetic induction data. In this example, the ocean is assumed to be composed of seawater. The combination of static gravity and magnetic induction measurements enables a better characterization of the hydrosphere by separately constraining the ice and ocean thicknesses.

the interior structure by modeling three different salts. Table 2 compares the ice thickness and ocean depth and conductivity obtained through our joint inversion with the different compositions.

For the case with the high induction amplitude the sensitivity to the ocean composition is negligible because the differences in the derived hydrosphere structure are well below the computed uncertainties. This is mainly due to the small range of ice thicknesses consistent with an induction response approaching that of a perfect conductor (see Figure S5 in Supporting Information S1). The resulting range of ocean conductivity derives from the high value of the amplitude, which requires values near saturation as discussed below. In the case with $A = 0.92$, the solutions obtained with different types of salts are still consistent within 1σ, but the differences among them are larger.

4. Discussion

Our approach is well-suited for a statistical study of the consistency among the different types of measurements used as constraints (e.g., Goossens et al., 2022). To validate our analysis, we compare the predictions of the

Table 2
Ice Thickness and Ocean Depth and Electrical Conductivity Derived by Assuming Different Chemical Compositions for the Ocean and Different Values of the Induction Amplitude (A = 0.97 ± 0.02 by Schilling et al. (2004) and A = 0.92 ± 0.02)

		Seawater	$MgSO_4$	Carbonates
$A = 0.97 \pm 0.02$	Ice thickness (km)	4^{+8}_{-3}	3^{+7}_{-2}	3^{+7}_{-2}
	Ocean depth (km)	133^{+21}_{-34}	134^{+21}_{-30}	136^{+22}_{-32}
	Ocean conductivity (S/m)	17^{+1}_{-5}	6^{+1}_{-2}	6^{+1}_{-1}
$A = 0.92 \pm 0.02$	Ice thickness (km)	24^{+11}_{-12}	14^{+11}_{-9}	20^{+12}_{-9}
	Ocean depth (km)	111^{+21}_{-30}	119^{+23}_{-28}	114^{+24}_{-29}
	Ocean conductivity (S/m)	16^{+1}_{-10}	4^{+1}_{-3}	5^{+1}_{-2}

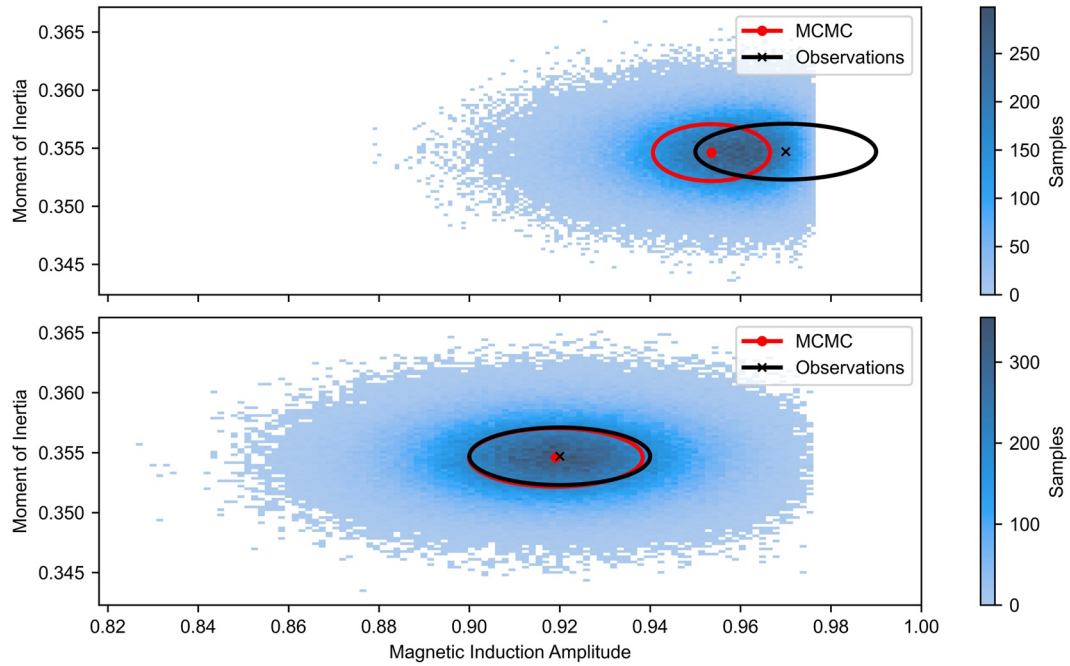

Figure 3. Posterior distributions of the moment of inertia (MoI) and induction amplitude generated by our methodology. The observations are the MoI from Gomez Casajus et al. (2021) with (a) $A = 0.97 \pm 0.02$ (Schilling et al., 2004) and (b) $A = 0.92 \pm 0.02$.

observations from the posteriors estimated by the MCMC with the probability distributions of the observations, which are assumed to be Gaussian. We obtain the probability distribution for mass, MoI, and induction amplitude by computing the mean and standard deviation of their distributions resulting from the MCMC. In Figure 3, we compare the estimated distributions and the observations for the MoI from Gomez Casajus et al. (2021) with the induction amplitude from Schilling et al. (2004) (Figure 3a), and the same MoI with a lower amplitude ($A = 0.92$, Figure 3b). Each point in the figure represents a draw from the MCMC. The observations ellipse (black line) is centered on the observed value, and its axes are defined by the measurement uncertainty. The estimated posterior ellipse (red line) center and axes are determined by the computed mean and standard deviation of the posterior distributions, respectively. Although all the models are consistent with the measurements in both cases, the solution with the high induction amplitude ($A = 0.97 \pm 0.02$) shows a significant bias with respect to the observations since models with $A > 0.98$ are only obtained with extremely high electrical conductivity (i.e., $\sigma > 100$ S/m for an ice thickness of 5 km; ocean thickness of 131 km to match the hydrosphere thickness prescribed by gravity data, Figure 1). In our models the upper limit on the electrical conductivity is set by salt saturation, which occurs for $\sim 304\, g_{NaCl}/kg_{H_2O}$ for seawater and $\sim 282\, g_{MgSO_4}/kg_{H_2O}$ for $MgSO_4$, corresponding to ~18 S/m and ~6 S/m, respectively (Hand & Chyba, 2007). For solutions of carbonates, sodium carbonate is the most soluble but reaches saturation for a concentration of 70 g/L at 0°C and about 110 g/L at 5°C (Kobe & Sheehy, 1948), which corresponds to conductivity of about ~3.5 S/m and ~6 S/m, respectively. Warmer mean temperatures are not expected in ocean worlds (e.g., Kang, 2022). Figure S5 in Supporting Information S1 shows how the saturation affects the maximum value of the induction amplitude. The conductivity values at saturation for the three compositions that we modeled are much lower than the conductivity that enables an induction amplitude greater than 0.98. We note that, in addition to the limits given by the compositional constraints that we introduced, the probability distribution of the induction amplitude ($A = 0.97 \pm 0.02$) implies that our MCMC should map values of the amplitude greater than 1, which are unphysical in our induction modeling. On the other hand, the lower induction amplitude $A = 0.92$ does not require very high electrical conductivity (i.e., ~4 S/m for a 20 km thick ice shell), and the inversion algorithm is able to better map the parameter space and reproduce the observations, showing that a lower value is both more aligned with thermal constraints and consistent with a broad range of plausible compositions.

Although available data do not constrain the ocean composition, future observations will help in disentangling the effects of the different types of salts on the data to distinguish between different ocean models. The tidal Love

numbers describe the response of the moon's interior structure to the tides exerted by the central planet, and show a large sensitivity to the ocean's density (e.g., Mitri et al., 2014). Integrating these measurements into the analysis will provide constraints on the ocean's density. Additionally, including multi-frequency induction measurements will constrain the ocean's electrical conductivity (e.g., Khurana et al., 2002; Vance et al., 2021). Combining these measurements and linking them through compositional constraints will be key to inferring the ocean's chemical composition.

5. Summary

We developed a technique for the inversion of icy moon interior structures based on the combination of gravity and magnetic field measurements and we applied it to data acquired by the Galileo mission during its flybys of Europa. We showed that this technique can disentangle the properties of the ice shell from those of the ocean, improving the characterization of icy moon hydrospheres. The methodology developed in this work provides a framework for analyzing and interpreting measurements that will be collected by future missions, leveraging synergies between different instruments and investigations. The Europa Clipper and JUICE missions are each expected to arrive in the Jupiter system in the 2030s, and will measure the gravity and magnetic fields of Europa, Ganymede, and Callisto. In addition to the mass, MoI, and induced magnetic field, these missions will provide observations of other geophysical parameters that can be integrated in our methodology. The tidal Love number k_2 will be measured for the three moons (Cappuccio et al., 2020, 2022; Mazarico et al., 2023) and will provide independent constraints on the density and rheological structure of the hydrosphere. The tidal Love number h_2 that quantifies the radial deformations will be measured with radar or laser altimeters at Europa (Steinbrügge et al., 2018) and Ganymede (Steinbrügge et al., 2015), providing complementary information to k_2. The combination of h_2 and k_2 is sensitive to the ice thickness (Wahr et al., 2006), further constraining the properties of the hydrosphere. Our method can also be extended by accounting for the amplitude parameters and the phase delay of the magnetic induction response at multiple frequencies, including those associated with the second harmonic of the synodic frequency and with the orbital frequency (e.g., Biersteker et al., 2023). Combining these future measurements self-consistently with compositional constraints through accurate experimental data will be fundamental in identifying the ocean's composition and unraveling the secrets of icy moon interior structures and composition.

Data Availability Statement

Input for the modeling and measurements of the geophysical parameters are taken from Anderson et al. (1998); Schilling et al. (2004); Gomez Casajus et al. (2021). The code used to generate the models is based on Genova et al. (2019).

Acknowledgments
F.P. and A.G. acknowledge funding from the Italian Space Agency (ASI) under contract 2021-19-HH.0. M.J.S. was supported by an appointment to the NASA Postdoctoral Program at the Jet Propulsion Laboratory, California Institute of Technology, administered by Oak Ridge Associated Universities under a contract with NASA (80HQTR21CA005). The contributions from J.C.-R., M.J.S., C.J.C., and S.D.V. were carried out at the Jet Propulsion Laboratory, California Institute of Technology, under a contract with NASA (80NM0018D0004).

References

Abdulagatov, I. M., Azizov, N. D., & Zeinalova, A. B. (2007). Viscosities, densities, apparent and partial molar volumes of concentrated aqueous $MgSO_4$ solutions at high temperatures and high pressures. *Physics and Chemistry of Liquids*, *45*(2), 127–148. https://doi.org/10.1080/00319100601089802

Anderson, J. D., Lau, E. L., Sjogren, W. L., Schubert, G., & Moore, W. B. (1996). Gravitational constraints on the internal structure of Ganymede. *Nature*, *384*(6609), 541–543. https://doi.org/10.1038/384541a0

Anderson, J. D., Schubert, G., Jacobson, R. A., Lau, E. L., Moore, W. B., & Sjogren, W. L. (1998). Europa's differentiated internal structure: Inferences from four Galileo encounters. *Science*, *281*(5385), 2019–2022. https://doi.org/10.1126/science.281.5385.2019

Biersteker, J. B., Weiss, B. P., Cochrane, C. J., Harris, C. D. K., Jia, X., Khurana, K. K., et al. (2023). Revealing the interior structure of icy moons with a Bayesian approach to magnetic induction measurements. *The Planetary Science Journal*, *4*(4), 62. https://doi.org/10.3847/PSJ/acc331

Cappuccio, P., Di Benedetto, M., Durante, D., & Iess, L. (2022). Callisto and Europa gravity measurements from JUICE 3GM experiment simulation. *The Planetary Science Journal*, *3*(8), 199. https://doi.org/10.3847/PSJ/ac83c4

Cappuccio, P., Hickey, A., Durante, D., Di Benedetto, M., Iess, L., De Marchi, F., et al.et al. (2020). Ganymede's gravity, tides and rotational state from JUICE's 3GM experiment simulation. *Planetary and Space Science*, *187*, 104902. https://doi.org/10.1016/j.pss.2020.104902

Castillo-Rogez, J. C., Daswani, M. M., Glein, C. R., Vance, S. D., & Cochrane, C. J. (2022). Contribution of non-water ices to salinity and electrical conductivity in ocean worlds. *Geophysical Research Letters*, *49*(16), e2021GL097256. https://doi.org/10.1029/2021GL097256

Durante, D., Hemingway, D., Racioppa, P., Iess, L., & Stevenson, D. (2019). Titan's gravity field and interior structure after Cassini. *Icarus*, *326*, 123–132. https://doi.org/10.1016/j.icarus.2019.03.003

Fukusako, S. (1990). Thermophysical properties of ice, snow, and sea ice. *International Journal of Thermophysics*, *11*(2), 353–372. https://doi.org/10.1007/BF01133567

Gelman, A., & Rubin, D. B. (1992). Inference from iterative simulation using multiple sequences. *Statistical Science*, *7*(4), 457–472. https://doi.org/10.1214/ss/1177011136

Genova, A., Goossens, S., Mazarico, E., Lemoine, F. G., Neumann, G. A., Kuang, W., et al. (2019). Geodetic evidence that Mercury has a solid inner core. *Geophysical Research Letters*, *46*(7), 3625–3633. https://doi.org/10.1029/2018GL081135

Gomez Casajus, L., Ermakov, A. I., Zannoni, M., Keane, J. T., Stevenson, D., Buccino, D. R., et al. (2022). Gravity field of Ganymede after the Juno Extended Mission. *Geophysical Research Letters*, *49*(24), e2022GL099475. https://doi.org/10.1029/2022GL099475

Gomez Casajus, L., Zannoni, M., Modenini, D., Tortora, P., Nimmo, F., Van Hoolst, T., et al. (2021). Updated Europa gravity field and interior structure from a reanalysis of Galileo tracking data. *Icarus*, *358*, 114187. https://doi.org/10.1016/j.icarus.2020.114187

Goossens, S., Renaud, J. P., Henning, W. G., Mazarico, E., Bertone, S., & Genova, A. (2022). Evaluation of recent measurements of Mercury's moments of inertia and tides using a comprehensive Markov Chain Monte Carlo method. *The Planetary Science Journal*, *3*(2), 37. https://doi.org/10.3847/PSJ/ac4bb8

Hand, K. P., & Chyba, C. F. (2007). Empirical constraints on the salinity of the europan ocean and implications for a thin ice shell. *Icarus*, *189*(2), 424–438. https://doi.org/10.1016/j.icarus.2007.02.002

Hastings, W. K. (1970). Monte Carlo sampling methods using Markov chains and their applications. *Biometrika*, *57*(1), 97–109. https://doi.org/10.1093/biomet/57.1.97

Howell, S. M. (2021). The likely thickness of Europa's icy shell. *The Planetary Science Journal*, *2*(4), 129. https://doi.org/10.3847/PSJ/abfe10

Hussmann, H., Spohn, T., & Wieczerkowski, K. (2002). Thermal equilibrium states of Europa's ice shell: Implications for internal ocean thickness and surface heat flow. *Icarus*, *156*(1), 143–151. https://doi.org/10.1006/icar.2001.6776

Iess, L., Rappaport, N. J., Jacobson, R. A., Racioppa, P., Stevenson, D. J., Tortora, P., et al. (2010). Gravity field, shape, and moment of inertia of Titan. *Science*, *327*(5971), 1367–1369. https://doi.org/10.1126/science.1182583

Kang, W. (2022). Different ice-shell geometries on europa and enceladus due to their different sizes: Impacts of ocean heat transport. *The Astrophysical Journal*, *934*(2), 116. https://doi.org/10.3847/1538-4357/ac779c

Kargel, J. S., Kaye, J. Z., Head, J. W., Marion, G. M., Sassen, R., Crowley, J. K., et al. (2000). Europa's crust and ocean: Origin, composition, and the prospects for life. *Icarus*, *148*(1), 226–265. https://doi.org/10.1006/icar.2000.6471

Khurana, K. K., Kivelson, M. G., & Russell, C. T. (2002). Searching for liquid water in Europa by using surface observatories. *Astrobiology*, *2*(1), 93–103. https://doi.org/10.1089/153110702753621376

Khurana, K. K., Kivelson, M. G., Stevenson, D. J., Schubert, G., Russell, C. T., Walker, R. J., & Polanskey, C. (1998). Induced magnetic fields as evidence for subsurface oceans in Europa and Callisto. *Nature*, *395*(6704), 777–780. https://doi.org/10.1038/27394

Kivelson, M. G., Khurana, K. K., Russell, C. T., Volwerk, M., Walker, R. J., & Zimmer, C. (2000). Galileo magnetometer measurements: A stronger case for a subsurface ocean at Europa. *Science*, *289*(5483), 1340–1343. https://doi.org/10.1126/science.289.5483.1340

Kivelson, M. G., Khurana, K. K., & Volwerk, M. (2002). The permanent and inductive magnetic moments of Ganymede. *Icarus*, *157*(2), 507–522. https://doi.org/10.1006/icar.2002.6834

Kobe, K. A., & Sheehy, T. M. (1948). Thermochemistry of sodium carbonate and its solutions. *Industrial & Engineering Chemistry*, *40*(1), 99–102. https://doi.org/10.1021/ie50457a029

Kuskov, O. L., & Kronrod, V. A. (2005). Internal structure of Europa and Callisto. *Icarus*, *177*(2), 550–569. https://doi.org/10.1016/j.icarus.2005.04.014

Matsuyama, I., Nimmo, F., Keane, J. T., Chan, N. H., Taylor, G. J., Wieczorek, M. A., et al. (2016). GRAIL, LLR, and LOLA constraints on the interior structure of the Moon. *Geophysical Research Letters*, *43*(16), 8365–8375. https://doi.org/10.1002/2016GL069952

Mazarico, E., Buccino, D., Castillo-Rogez, J., Dombard, A. J., Genova, A., Hussmann, H., et al. (2023). The Europa clipper gravity and radio science investigation. *Space Science Reviews*, *219*(4), 30. https://doi.org/10.1007/s11214-023-00972-0

Metropolis, N., Rosenbluth, A. W., Rosenbluth, M. N., Teller, A. H., & Teller, E. (1953). Equation of state calculations by fast computing machines. *The Journal of Chemical Physics*, *21*(6), 1087–1092. https://doi.org/10.1063/1.1699114

Millero, F. J., Feistel, R., Wright, D. G., & McDougall, T. J. (2008). The composition of standard seawater and the definition of the reference-composition salinity scale. *Deep Sea Research Part I: Oceanographic Research Papers*, *55*(1), 50–72. https://doi.org/10.1016/j.dsr.2007.10.001

Mitri, G., Meriggiola, R., Hayes, A., Lefevre, A., Tobie, G., Genova, A., et al. (2014). Shape, topography, gravity anomalies and tidal deformation of Titan. *Icarus*, *236*, 169–177. https://doi.org/10.1016/j.icarus.2014.03.018

Ojakangas, G. W., & Stevenson, D. J. (1989). Thermal state of an ice shell on Europa. *Icarus*, *81*(2), 220–241. https://doi.org/10.1016/0019-1035(89)90052-3

Parkinson, W. D. (1983). *Introduction to Geomagnetism*. Scottish Academic Press.

Poisson, A. (1980). Conductivity/salinity/temperature relationship of diluted and concentrated standard seawater. *IEEE Journal of Oceanic Engineering*, *5*(1), 41–50. https://doi.org/10.1109/JOE.1980.1145442

Pozzo, M., Davies, C., Gubbins, D., & Alfè, D. (2012). Thermal and electrical conductivity of iron at Earth's core conditions. *Nature*, *485*(7398), 355–358. https://doi.org/10.1038/nature11031

Ruesch, O., Genova, A., Neumann, W., Quick, L. C., Castillo-Rogez, J. C., Raymond, C. A., et al. (2019). Slurry extrusion on Ceres from a convective mud-bearing mantle. *Nature Geoscience*, *12*(7), 505–509. https://doi.org/10.1038/s41561-019-0378-7

Saur, J., Duling, S., Roth, L., Jia, X., Strobel, D. F., Feldman, P. D., et al. (2015). The search for a subsurface ocean in Ganymede with Hubble Space Telescope observations of its auroral ovals. *Journal of Geophysical Research: Space Physics*, *120*(3), 1715–1737. https://doi.org/10.1002/2014JA020778

Schilling, N., Khurana, K. K., & Kivelson, M. G. (2004). Limits on an intrinsic dipole moment in Europa. *Journal of Geophysical Research*, *109*(5), E05006. https://doi.org/10.1029/2003JE002166

Seufert, M., Saur, J., & Neubauer, F. M. (2011). Multi-frequency electromagnetic sounding of the Galilean moons. *Icarus*, *214*(2), 477–494. https://doi.org/10.1016/j.icarus.2011.03.017

Sohl, F., Spohn, T., Breuer, D., & Nagel, K. (2002). Implications from Galileo observations on the interior structure and chemistry of the Galilean satellites. *Icarus*, *157*(1), 104–119. https://doi.org/10.1006/icar.2002.6828

Steinbrügge, G., Schroeder, D., Haynes, M., Hussmann, H., Grima, C., & Blankenship, D. (2018). Assessing the potential for measuring Europa's tidal Love number h2 using radar sounder and topographic imager data. *Earth and Planetary Science Letters*, *482*, 334–341. https://doi.org/10.1016/j.epsl.2017.11.028

Steinbrügge, G., Stark, A., Hussmann, H., Sohl, F., & Oberst, J. (2015). Measuring tidal deformations by laser altimetry. A performance model for the Ganymede Laser Altimeter. *Planetary and Space Science*, *117*, 184–191. https://doi.org/10.1016/j.pss.2015.06.013

Styczinski, M. J., Vance, S. D., Harnett, E. M., & Cochrane, C. J. (2022). A perturbation method for evaluating the magnetic field induced from an arbitrary, asymmetric ocean world analytically. *Icarus*, *376*, 114840. https://doi.org/10.1016/j.icarus.2021.114840

Tobie, G., Mocquet, A., & Sotin, C. (2005). Tidal dissipation within large icy satellites: Applications to Europa and Titan. *Icarus*, *177*(2), 534–549. https://doi.org/10.1016/j.icarus.2005.04.006

Vance, S. D., Styczinski, M. J., Bills, B. G., Cochrane, C. J., Soderlund, K. M., Gómez-Pérez, N., & Paty, C. (2021). Magnetic induction responses of Jupiter's ocean moons including effects from adiabatic convection. *Journal of Geophysical Research: Planets*, *126*(2), e2020JE006418. https://doi.org/10.1029/2020JE006418

Wahr, J. M., Zuber, M. T., Smith, D. E., & Lunine, J. I. (2006). Tides on Europa, and the thickness of Europa's icy shell. *Journal of Geophysical Research*, *111*(12), E12005. https://doi.org/10.1029/2006JE002729

Zimmer, C., Khurana, K. K., & Kivelson, M. G. (2000). Subsurface oceans on Europa and Callisto: Constraints from Galileo magnetometer observations. *Icarus*, *147*(2), 329–347. https://doi.org/10.1006/icar.2000.6456

Zolotov, M. Y., & Shock, E. L. (2001). Composition and stability of salts on the surface of Europa and their oceanic origin. *Journal of Geophysical Research*, *106*(E12), 32815–32827. https://doi.org/10.1029/2000JE001413